


# Modeling optical absorption for thermoreflectance measurements

Cite as: J. Appl. Phys. **119**, 095107 (2016); <https://doi.org/10.1063/1.4943176>

Submitted: 06 November 2015 . Accepted: 21 February 2016 . Published Online: 07 March 2016

Jia Yang, Elbara Ziade, and  Aaron J. Schmidt



View Online



Export Citation



CrossMark

## ARTICLES YOU MAY BE INTERESTED IN

[A frequency-domain thermoreflectance method for the characterization of thermal properties](#)  
Review of Scientific Instruments **80**, 094901 (2009); <https://doi.org/10.1063/1.3212673>

[Analysis of heat flow in layered structures for time-domain thermoreflectance](#)  
Review of Scientific Instruments **75**, 5119 (2004); <https://doi.org/10.1063/1.1819431>

[Uncertainty analysis of thermoreflectance measurements](#)  
Review of Scientific Instruments **87**, 014901 (2016); <https://doi.org/10.1063/1.4939671>



## Your Qubits. Measured.

Meet the next generation of quantum analyzers

- Readout for up to 64 qubits
- Operation at up to 8.5 GHz, mixer-calibration-free
- Signal optimization with minimal latency

Find out more



# Modeling optical absorption for thermoreflectance measurements

Jia Yang, Elbara Ziade, and Aaron J. Schmidt

*Department of Mechanical Engineering, Boston University, Boston, Massachusetts 02215, USA*

(Received 6 November 2015; accepted 21 February 2016; published online 7 March 2016)

Optical pump-probe techniques based on thermoreflectance, such as time domain thermoreflectance and frequency domain thermoreflectance (FDTR), have been widely used to characterize the thermal conductivity of thin films and the thermal conductance across interfaces. These techniques typically use a transducer layer to absorb the pump light and improve the thermoreflectance signal. The transducer, however, complicates the interpretation of the measured signal because the approximation that all the energy from the pump beam is deposited at the transducer surface is not always accurate. In this paper, we consider the effect of laser absorption in the top layer of a multilayer sample, and derive an analytical solution for the thermoreflectance signal in the diffusion regime based on volumetric heating. We analyze the measurement sensitivity to the pump absorption depth for transducers with different thermal conductivities, and investigate the additional effect of probe laser penetration depth on the measured signal. We validate our model using FDTR measurements on 490 nm thick amorphous silicon films deposited on fused silica and silicon substrates. © 2016 AIP Publishing LLC. [<http://dx.doi.org/10.1063/1.4943176>]

## I. INTRODUCTION

Heat transfer at the nanoscale has been a primary concern in the development of technologies such as nanoelectronics and thermoelectric energy conversion devices.<sup>1</sup> This has motivated the development of metrology techniques that can probe thermal transport in nanoscale systems. Measurements based on pump-probe thermoreflectance, such as time domain thermoreflectance (TDTR)<sup>2–4</sup> and frequency domain thermoreflectance (FDTR),<sup>5</sup> have allowed researchers to study thermal transport on experimental length and timescales comparable to energy carrier mean free paths (MFPs), and have been widely used to characterize the thermal conductivity of nanoscale thin films<sup>6–8</sup> and the thermal conductance across interfaces.<sup>9–11</sup> Furthermore, by changing the optical spot size<sup>12,13</sup> or increasing the heating frequency up to 200 MHz,<sup>14</sup> TDTR and FDTR have been used to estimate the mean free path distribution of thermal energy carriers, which is a critical step towards engineering the thermal conductivity of nanostructured materials.

Thermoreflectance techniques typically make use of a transducer layer that is deposited onto the sample.<sup>15–17</sup> The purpose of the transducer is to absorb and convert the pump light into heat at the sample surface, and to produce a measurable thermal signal by possessing a large coefficient of thermoreflectance at the probe laser wavelength. The drawback of using a transducer layer is that it requires the experimenter to modify the sample. In addition, while the absorbed pump light in the transducer is commonly modeled as a surface heat source,<sup>4</sup> the approximation that all of the energy from the pump beam is deposited at the sample surface is not always accurate. For example, weak electron-phonon coupling can extend the location where the laser energy is deposited into a metal transducer and may have a significant impact on high frequency FDTR signals,<sup>18,19</sup> and a recent study by Collins *et al.* on the frequency domain representation of TDTR data showed that adjusting the energy absorption depth in the

transducer layer changed the fitting results.<sup>20</sup> Moreover, low thermal conductivity transducers provide greater sensitivity for studying in-plane thermal transport in anisotropic materials,<sup>21</sup> superlattices,<sup>22</sup> and two-dimensional materials,<sup>23</sup> but they can experience a significant temperature gradient within the absorption depth of the pump light. Therefore, accurately modeling the energy absorption in the transducer is important for interpreting thermoreflectance measurements.

In this paper, we consider pump laser absorption in the top layer of a multilayer sample during thermoreflectance measurements, and derive an analytical solution for the thermoreflectance signal in the diffusion regime based on volumetric heating. We analyze the measurement sensitivity to the pump absorption depth for transducers with different thermal conductivities. In addition, we investigate the effect of the probe laser penetration depth on the measured signal. We validate our model using FDTR measurements of a 490 nm thick amorphous silicon (aSi) film deposited on fused silica and silicon substrates.

## II. EXPERIMENTAL ANALYSIS OF TDTR AND FDTR

Details on the implementations of the TDTR and FDTR techniques can be found elsewhere.<sup>1,5</sup> Here we focus on deriving an analytical heat transfer model in the diffusion regime, considering the pump laser beam as a volumetric heat source. This model is then inserted into the standard signal analysis procedure for TDTR and FDTR experiments. In FDTR, the pump beam is modulated at multiple frequencies, while a lock-in amplifier records the phase lag between the pump beam and probe beam at each frequency. In TDTR, the pump and probe beams originate from a pulsed laser source, such as an ultrafast Ti:sapphire laser oscillator, and are separated by a variable optical delay. The pump pulses heat the sample, while the probe pulses measure the surface temperature as a function of the optical delay. The pump beam is typically given an additional periodic modulation at

a single frequency to enable lock-in detection. For either case, the probe signal detected by the lock-in amplifier at the modulation frequency  $\omega$  can be represented by

$$A(\omega) \exp[i(\omega t + \phi(\omega))] = Z(\omega) \exp(i\omega t), \quad (1)$$

where  $A(\omega)$  is the amplitude,  $\phi(\omega)$  is the phase lag, and  $Z(\omega)$  is a complex number that represents the frequency response of the experimental situation. The unknown thermal properties of the sample are then obtained by minimizing the difference between the measured phase data and the values calculated with a model for  $Z(\omega)$ .

For the case of FDTR with continuous-wave (cw) lasers

$$Z(\omega) = \beta H(\omega), \quad (2)$$

where  $\beta$  is a constant and  $H(\omega)$  is the frequency response of the sample surface temperature weighted by the intensity distribution of the probe beam. The constant  $\beta$  is given by

$$\beta = \frac{1}{2} \dot{Q}_{\text{pump}} \dot{Q}_{\text{probe}} (1 - R_{\lambda_{\text{pump}}}) \left( \frac{dR}{dT} \right)_{\lambda_{\text{probe}}} G_{\text{det}}, \quad (3)$$

where  $\dot{Q}_{\text{pump}}$  is the output power of the cw pump laser,  $\dot{Q}_{\text{probe}}$  is the cw probe laser power that is impinging on the sample surface,  $R_{\lambda_{\text{pump}}}$  is surface reflectivity at the pump wavelength,  $\frac{dR}{dT}$  is the thermoreflectance coefficient at the probe wavelength, and  $G_{\text{det}}$  is the product of the photodetector gain and the photodiode responsivity at the probe wavelength.

For the case of TDTR

$$Z(\omega) = \beta \sum_{k=-\infty}^{\infty} H(\omega + k\omega_s) \exp(ik\omega_s \tau), \quad (4)$$

where  $\tau$  is the delay time between pump and probe pulses,  $\omega_s$  is the angular laser pulsing frequency, and  $H(\omega + k\omega_s)$  is the same frequency domain solution for the sample surface temperature as in Eq. (2).<sup>24</sup> The constant  $\beta$  is still given by Eq. (3), where now  $\dot{Q}_{\text{pump}} = Q_{\text{pump}} \cdot \omega_s / 2\pi$  and  $\dot{Q}_{\text{probe}} = Q_{\text{probe}} \cdot \omega_s / 2\pi$ , where  $Q_{\text{pump}}$  and  $Q_{\text{probe}}$  are the energy per pulse in the pump and probe beams, respectively. Next we present an analytical model for  $H(\omega)$  considering a multilayer stack of materials where the pump laser is modeled as an exponentially decaying volumetric heat source.

### III. HEAT TRANSFER ANALYSIS

#### A. Limits of the model

The measurement configuration for a multilayer sample is shown in Fig. 1. A periodically modulated pump laser locally heats the sample, while an unmodulated probe laser monitors the surface temperature through a proportional change in reflectivity. The first layer serves as the thermoreflectance transducer and is typically a thin metal film, although the analysis here applies to any top layer that absorbs the pump light.

In our analysis, we assume that all heat carriers, such as electrons and phonons, are in local thermal equilibrium and are well described by a diffusion model. Under this condition, the MFPs of the heat carriers should be smaller than the length scales in the measurement, which include the focused laser

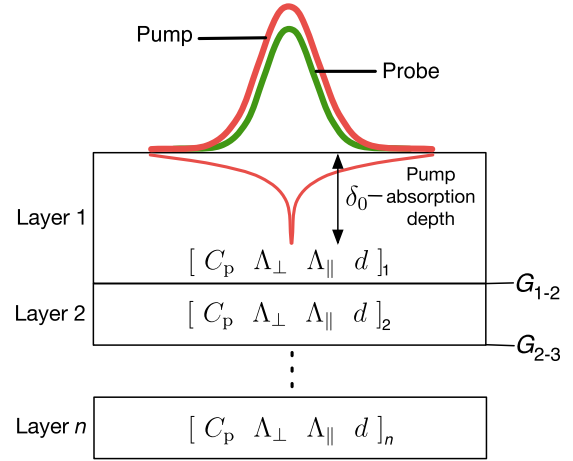


FIG. 1. Schematic of a multilayer sample during a pump-probe thermoreflectance measurement. The pump laser deposits energy into the first layer with a  $1/e$  absorption depth,  $\delta_0$ . Each layer is described by a volumetric heat capacity,  $C_p$ , the cross-plane and in-plane thermal conductivity,  $\Lambda_{\perp}$  and  $\Lambda_{\parallel}$ , and the thermal boundary conductance to the next layer,  $G$ .

spot sizes, the optical absorption depth, and the thermal penetration depth of the heat source. In addition, the experimental timescale (the time between laser pulses for TDTR, or the heating period in FDTR) should be longer than the electron-phonon equilibrium time. Our model is not valid in cases where the MFPs of the heat carriers are longer than the relevant length scales, such as the Ballistic transport in pure crystals,<sup>12,14,18</sup> materials at low temperatures,<sup>12</sup> and materials with weak electron-phonon coupling.<sup>19,25,26</sup> In these situations, a two-temperature model<sup>19,25</sup> or a model that accounts for Ballistic transport such as the Boltzmann transport equation is needed to accurately describe the nonequilibrium heat flow.

In our analysis, we further assume that all the heat is deposited where the pump light is absorbed. According to the Beer-Lambert law, when the pump laser is impinging on a material surface, the optical intensity is reduced to  $1/e$  of the total intensity at the optical absorption depth,  $\delta_0$ . The pump irradiation excites hot electrons that travel a distance  $L_e$  before thermalizing with phonons. When  $L_e$  is greater than  $\delta_0$ , electrons can travel a significant distance before thermalizing and the optical absorption depth becomes an inaccurate representation of the depth of the heat source. Additionally,  $L_e$  must be much less than the laser spot size or radial spreading of hot electrons will change the size of the heating area and invalidate the analysis. Our model also does not apply to situations where photo-generated electron-hole pairs can travel a significant distance before depositing their energy, such as high quality semiconductor crystals. Next we estimate values of  $L_e$  for several conductive materials to identify when the assumption of local heat deposition is appropriate.

We calculate  $L_e$  for gold, aluminum, and nickel and compare them to the materials' optical absorption depth for a wavelength of 785 nm.  $L_e$  can be estimated from

$$L_e = \sqrt{\frac{\Lambda_e \cdot \tau_{e,ph}}{C_e}}, \quad (5)$$

where  $\Lambda_e$  and  $C_e$  are the electronic contributions to the thermal conductivity and heat capacity, respectively, and  $\tau_{e,ph}$  is

TABLE I. Values used to calculate  $L_e$  for Au, Al, and Ni. Our optical absorption model becomes accurate as  $L_e$  approaches  $\delta_0$ .

Material	$\Lambda_e$ (W m <sup>-1</sup> K <sup>-1</sup> )	$C_e$ (kJ m <sup>-3</sup> K <sup>-1</sup> )	$\tau_{e,ph}$ (fs)	$L_e$ (nm)	$\delta_0$ (nm)
Au, bulk	333 (Ref. 27)	20.3 (Ref. 27)	830 (Ref. 28)	117	12.8 (Ref. 31)
Au, 100 nm	250 (Ref. 6)	20.3 (Ref. 27)	830 (Ref. 28)	101	12.8 (Ref. 31)
Al, bulk	267 (Ref. 27)	40.5 (Ref. 27)	550 (Ref. 29)	60.2	7.3 (Ref. 31)
Al, 100 nm	120 (Ref. 6)	40.5 (Ref. 27)	550 (Ref. 29)	40.4	7.3 (Ref. 31)
Ni, bulk	105 (Ref. 27)	323.2 (Ref. 27)	400 (Ref. 30)	11.4	14.5 (Ref. 31)

the electron-phonon thermalization time. We calculated the bulk values of  $\Lambda_e$  using the Wiedemann-Franz law with electrical conductivity values taken from Ref. 27 and a Lorentz number of  $2.44 \times 10^{-8} \text{ W}\Omega\text{K}^{-2}$ .  $C_e$  was calculated with the room temperature electron heat capacity coefficients given in Ref. 27. Values for  $\tau_{e,ph}$  were obtained from the literature for gold,<sup>28</sup> aluminum,<sup>29</sup> and nickel.<sup>30</sup> We calculated the optical absorption depth from  $\delta_0 = \lambda/(4\pi\kappa)$ , where  $\kappa$  is the imaginary part of the material's index of refraction at a pump laser wavelength of  $\lambda = 785 \text{ nm}$ .<sup>31</sup> We also included the values for 100 nm gold and 100 nm aluminum which are typically used as transducers in thermoreflectance measurements.<sup>4,34</sup> The  $\Lambda_e$  values for these two thin films are taken from Ref. 6. The calculated values of  $L_e$  and  $\delta_0$ , along with  $\Lambda_e$ ,  $C_e$ , and  $\tau_{e,ph}$ , are listed in Table I. We see that the electron diffusion length decreases with electrical conductivity for the three investigated metals. For gold and aluminum,  $L_e$  is greater than  $\delta_0$ , indicating that our absorption model will not accurately represent the true heating profile of the pump laser, while for Ni  $L_e$  is less than  $\delta_0$  and the geometry of the heat source should closely match the intensity profile of the pump light.

We further investigate the effect of electron diffusion by solving the one-dimensional (1D) heat diffusion equation for electrons in a semi-infinite solid heated by the pump laser. The solution was used to calculate the electron temperature profiles for the three metals and compare them to the temperature profiles obtained by assuming that the heat is deposited exactly where the pump light is absorbed. We let the pump laser with a power of  $P(t)$  impinge on an area  $A$  on the surface of a semi-infinite solid. We assume that the linear dimensions of  $A$  are large compared to  $\delta_0$  and  $L_e$ , so that the 1D heat diffusion equation for the electrons is valid

$$\Lambda_e \frac{\partial^2 \theta}{\partial z^2} + \frac{P(t)}{A\delta_0} \exp\left(-\frac{z}{\delta_0}\right) = C_e \frac{\partial \theta}{\partial t}, \quad (6)$$

where  $\theta$  is the electron temperature. In the frequency domain, this becomes

$$\Lambda_e \frac{\partial^2 \theta(\omega)}{\partial z^2} + \frac{P(\omega)}{A\delta_0} \exp\left(-\frac{z}{\delta_0}\right) = i\omega C_e \theta(\omega), \quad (7)$$

where  $P(\omega)$  is the Fourier transform of  $P(t)$ . Solving Eq. (7) with an adiabatic boundary condition at the top surface and a semi-infinite boundary condition at the bottom surface, we obtain

$$\theta(\omega, z) = \frac{P(\omega)}{A\delta_0} \cdot \frac{\exp(-qz) - q\delta_0 \exp\left(-\frac{z}{\delta_0}\right)}{\Lambda_e q (1 - q^2 \delta_0^2)}, \quad (8)$$

where  $q^2 = C_e i\omega/\Lambda_e$ .

We evaluate Eq. (8) at  $\omega = 2\pi/\tau_{e,ph}$  to estimate the electron temperature profile,  $\theta(z)$ , in the material when the electrons begin to equilibrate with the lattice. In Fig. 2 we plot  $\theta(z)$  for the three metals listed in Table I. We see that as the electronic diffusion length decreases, the electron temperature profile approaches the optical absorption profile, and that an exponentially decaying heat source is a good approximation when  $L_e \leq \delta_0$ . Therefore, the model we present in Section III B should be reasonably accurate for materials with low to moderate electrical conductivity. In addition to the bulk solutions, we also plot  $\theta(z)$  using values of  $\Lambda_e$  measured for 100 nm gold and 100 nm aluminum films made with electron beam deposition. The results suggest that the model may be a better approximation for thin films than bulk materials because of increased electrical resistivity in thin films. The model may also be qualitatively useful for understanding the impact of the optical absorption depth for materials with high electrical conductivity or weak electron-phonon coupling, but in these cases the effective absorption depth may be significantly larger than the optical absorption depth.

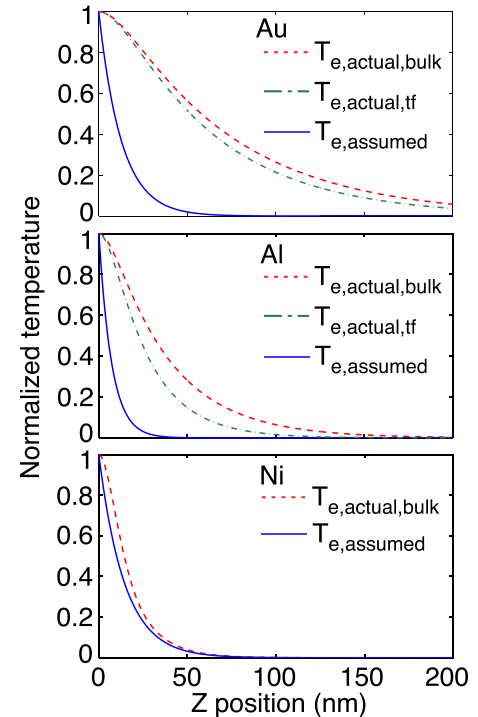


FIG. 2. Temperature profiles of the heat source assuming heat is deposited within the optical absorption profile (solid lines) and the calculated electron temperature profile for thermalized electrons using Eq. (8) (dashed lines). For gold and aluminum, electron temperature profiles are plotted using both bulk values ( $T_{e,actual,bulk}$ ) and thin film values ( $T_{e,actual,tf}$ ).

## B. Diffusion analysis

As shown in Fig. 1, we model each layer of the sample with a thickness,  $d$ , a volumetric heat capacity,  $C_p$ , a cross-plane and in-plane thermal conductivity,  $\Lambda_\perp$  and  $\Lambda_\parallel$ , respectively, and a thermal boundary conductance (TBC) to the next layer,  $G$ . We begin by analyzing the first layer of the sample. We assume that the pump laser is a Gaussian beam which is only absorbed in the first layer as a volumetric heat source according to

$$f_{\text{gen}}(r, z, t) = \frac{2P(t)}{\pi w_0^2 \delta_0 \left[ 1 - \exp\left(-\frac{d_1}{\delta_0}\right) \right]} \times \exp\left(-\frac{2r^2}{w_0^2}\right) \exp\left(-\frac{z}{\delta_0}\right), \quad (9)$$

where  $f_{\text{gen}}(r, z, t)$  is the volumetric heat generation at radial position  $r$  and depth below the sample surface  $z$ , and  $d_1$  is the thickness of the first layer. In Eq. (9),  $P(t)$  is the total absorbed pump power in the first layer as a function of time,  $w_0$  is the  $1/e^2$  radius of the focused pump spot on the surface, and  $\delta_0$  is the  $1/e$  optical absorption depth of the first layer at the pump laser wavelength. Here we assume negligible optical spreading within the distance of optical absorption because  $\delta_0$  is typically much less than  $w_0$ . The heat conduction in the layer including this heat generation term can be expressed in cylindrical coordinates as

$$\frac{\Lambda_r}{r} \frac{\partial}{\partial r} \left( r \frac{\partial \theta}{\partial r} \right) + \Lambda_z \frac{\partial^2 \theta}{\partial z^2} + \frac{2P(t)}{\pi w_0^2 \delta_0 \left[ 1 - \exp\left(-\frac{d_1}{\delta_0}\right) \right]} \times \exp\left(-\frac{2r^2}{w_0^2}\right) \exp\left(-\frac{z}{\delta_0}\right) = C_p \frac{\partial \theta}{\partial t}, \quad (10)$$

where  $\theta$  is the temperature,  $\Lambda_r$  and  $\Lambda_z$  are the in-plane and cross-plane thermal conductivities, respectively, and  $C_p$  is the volumetric heat capacity. We assume negligible convec-

tion or radiation to the surroundings, so that the heat flux boundary condition on the top surface is  $f_t = 0$ . We find the solution of Eq. (10) in the frequency domain following the approach described by Carslaw and Jaeger.<sup>32</sup> Taking the Fourier transform and Hankel transform of Eq. (10), we obtain

$$\Lambda_z \frac{\partial^2 \theta(\omega, k, z)}{\partial z^2} + \frac{P(\omega)}{2\pi \delta_0 \left[ 1 - \exp\left(-\frac{d_1}{\delta_0}\right) \right]} \times \exp\left(-\frac{k^2 w_0^2}{8}\right) \exp\left(-\frac{z}{\delta_0}\right) = (\Lambda_r k^2 + C_p i \omega) \theta(\omega, k, z), \quad (11)$$

where  $\omega$  is the angular frequency,  $k$  is the Hankel transform variable, and  $P(\omega)$  is the Fourier transform of  $P(t)$ . If we let

$$q^2 = \frac{\Lambda_r k^2 + C_p i \omega}{\Lambda_z},$$

and

$$T(\omega, k, z) = \theta(\omega, k, z) + \frac{P(\omega) \exp\left(-\frac{k^2 w_0^2}{8}\right) \delta_0}{2\pi \Lambda_z (1 - q^2 \delta_0^2) \left[ 1 - \exp\left(-\frac{d_1}{\delta_0}\right) \right]} \exp\left(-\frac{z}{\delta_0}\right),$$

then Eq. (11) can be written as

$$\frac{1}{q^2} \frac{\partial^2 T(\omega, k, z)}{\partial z^2} = T(\omega, k, z). \quad (12)$$

By solving Eq. (12) with the adiabatic surface boundary condition, we obtain the relationship between the top side temperature,  $\theta_{1,t}$ , and the bottom side temperature,  $\theta_{1,b}$ , and heat flux,  $f_{1,b}$ , in the frequency domain for the first layer through

$$\begin{pmatrix} \theta_{1,b} \\ f_{1,b} \end{pmatrix} = \begin{pmatrix} \cosh(qd_1) & \left( -\frac{\sinh(qd_1)}{\Lambda_z q} + \frac{\delta_0 \cosh(qd_1)}{\Lambda_z} - \frac{\delta_0}{\Lambda_z} \exp\left(-\frac{d_1}{\delta_0}\right) \right) \\ -\Lambda_z q \sinh(qd_1) & \left( \cosh(qd_1) - q \delta_0 \sinh(qd_1) - \exp\left(-\frac{d_1}{\delta_0}\right) \right) \end{pmatrix} \begin{pmatrix} \theta_{1,t} \\ \frac{P(\omega) \exp\left(-\frac{k^2 w_0^2}{8}\right)}{2\pi (1 - q^2 \delta_0^2) \left[ 1 - \exp\left(-\frac{d_1}{\delta_0}\right) \right]} \end{pmatrix}. \quad (13)$$

The diffusion equation for the remaining layers can be solved using a matrix method.<sup>4,24,32</sup> For a layer of material  $n$ , the temperature and heat flux on the top surface are related to the temperature and heat flux on the bottom surface

$$\begin{pmatrix} \theta_{n,b} \\ f_{n,b} \end{pmatrix} = \begin{pmatrix} \cosh(qd) & -\frac{\sinh(qd)}{\Lambda_z q} \\ -\Lambda_z q \sinh(qd) & \cosh(qd) \end{pmatrix} \begin{pmatrix} \theta_{n,t} \\ f_{n,t} \end{pmatrix}, \quad (14)$$

where  $d$  is the layer thickness and  $q$  is given by the same formula used in Eq. (13). A thermal boundary conductance  $G$  between the bottom surface of layer  $n$  to the top surface of the next layer  $n+1$  is included in the matrix multiplication as



$$\begin{pmatrix} \theta_{n+1,t} \\ f_{n+1,t} \end{pmatrix} = \begin{pmatrix} 1 & -G^{-1} \\ 0 & 1 \end{pmatrix} \begin{pmatrix} \theta_{n,b} \\ f_{n,b} \end{pmatrix}. \quad (15)$$

Combining Eq. (13) with Eqs. (14) and (15), we obtain the solution for a multilayer sample through matrix multiplication

$$\begin{pmatrix} \theta_b \\ f_b \end{pmatrix} = M_N M_{N-1} \cdots M_2 M_1 \times \begin{pmatrix} \theta_{1,t} \\ \frac{P(\omega) \exp\left(-\frac{k^2 w_0^2}{8}\right)}{2\pi(1 - q^2 \delta_0^2) \left[1 - \exp\left(\frac{-d_1}{\delta_0}\right)\right]} \end{pmatrix}, \quad (16)$$

where  $M_1$  is the matrix for the first layer from Eq. (13) and  $M_n$ ,  $n=2, \dots, N$  are the matrices for the remaining layers from Eqs. (14) and (15). We let

$$M_N M_{N-1} \cdots M_2 M_1 = \begin{pmatrix} A & B \\ C & D \end{pmatrix}.$$

Then if an adiabatic or semi-infinite boundary condition is applied to bottom surface of the  $N$ th layer, the surface temperature can be determined from Eq. (16) as

$$\theta_{1,t} = -\frac{D}{C} \frac{P(\omega)}{2\pi(1 - q^2 \delta_0^2) \left[1 - \exp\left(\frac{-d_1}{\delta_0}\right)\right]} \exp\left(-\frac{k^2 w_0^2}{8}\right). \quad (17)$$

By taking the inverse Hankel transform of Eq. (17), we obtain the temperature distribution in real space on the surface

$$\begin{aligned} \theta_{1,t}(\omega, r) = & \int_0^\infty k J_0(kr) \left(-\frac{D}{C}\right) \\ & \times \frac{P(\omega)}{2\pi(1 - q^2 \delta_0^2) \left[1 - \exp\left(\frac{-d_1}{\delta_0}\right)\right]} \exp\left(-\frac{k^2 w_0^2}{8}\right) dk. \end{aligned} \quad (18)$$

This temperature distribution is measured with the reflected probe beam as described in Section III C.

### C. Role of the probe beam

We first consider the case where it is assumed that the reflected probe beam measures the temperature at the sample surface, and then consider the more realistic case where the probe beam penetrates into the material. For the former case, the thermoreflectance signal is proportional to the surface temperature distribution weighted by the Gaussian intensity profile of the probe beam on the sample surface

$$\begin{aligned} \overline{\theta_{1,t}(\omega)} = & \frac{P(\omega)}{2\pi \left[1 - \exp\left(\frac{-d_1}{\delta_0}\right)\right]} \int_0^\infty k \left(-\frac{D}{C}\right) \frac{1}{1 - q^2 \delta_0^2} \\ & \times \exp\left[-\frac{k^2(w_0^2 + w_1^2)}{8}\right] dk, \end{aligned} \quad (19)$$

where  $w_1$  is the  $1/e^2$  radius of the probe beam spot on the surface. The frequency response of the sample,  $H(\omega)$ , which is inserted into Eq. (2) for an FDTR measurement and Eq. (4) for a TDTR measurement, is given by  $H(\omega) = \overline{\theta_{1,t}(\omega)}/P(\omega)$ , so that

$$\begin{aligned} H(\omega) = & \frac{1}{2\pi \left[1 - \exp\left(\frac{-d_1}{\delta_0}\right)\right]} \int_0^\infty k \left(-\frac{D}{C}\right) \frac{1}{1 - q^2 \delta_0^2} \\ & \times \exp\left[-\frac{k^2(w_0^2 + w_1^2)}{8}\right] dk. \end{aligned} \quad (20)$$

In the limit of  $\delta_0 = 0$ , Eq. (20) simplifies to the solution for surface heating given in Ref. 24.

We now examine the effect of the optical penetration depth of the probe beam,  $\delta_1$ . We consider a 1D semi-infinite solid heated by a periodically modulated pump laser and probed by a cw laser, as shown in Fig. 3. In general, the reflected probe signal can be modeled by solving Maxwell's equations in the material. In the frequency domain, the reflected probe signal can be written as<sup>33</sup>

$$\Delta R(\omega) = \int_0^\infty f(z) \theta(z, \omega) dz, \quad (21)$$

where  $\theta(z, \omega)$  is temperature in the sample and  $f(z)$  is a sensitivity function that is an exponentially damped oscillation with non-zero phase at the surface  $z = 0$

$$f(z) = f_0 \left[ \frac{\partial n}{\partial \theta} \sin\left(\frac{4\pi n z}{\lambda} - \psi\right) + \frac{\partial \kappa}{\partial \theta} \cos\left(\frac{4\pi n z}{\lambda} - \psi\right) \right] \exp\left(-\frac{z}{\delta_1}\right), \quad (22)$$

$$f_0 = 8 \frac{2\pi \left[ n^2(n^2 + \kappa^2 - 1)^2 + \kappa^2(n^2 + \kappa^2 + 1)^2 \right]^{1/2}}{\lambda \left[ (n+1)^2 + \kappa^2 \right]^2}, \quad (23)$$

$$\tan \psi = \frac{\kappa(n^2 + \kappa^2 + 1z)}{n(n^2 + \kappa^2 - 1)}. \quad (24)$$

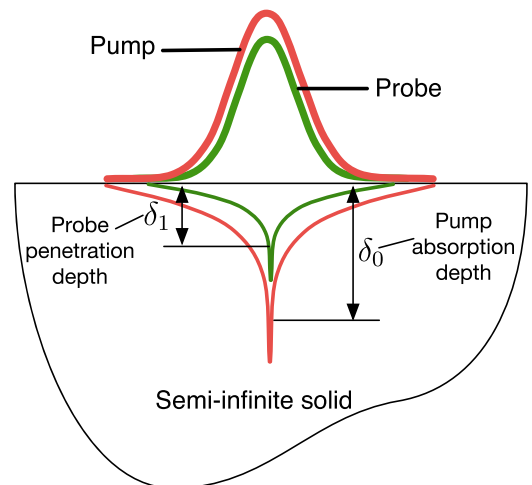


FIG. 3. Schematic of pump and probe absorption in a semi-infinite solid.

In Eq. (22),  $\lambda$  is the probe wavelength,  $\psi$  is a phase angle between 0 and  $\pi/2$ , and  $n$  and  $\kappa$  are the real and imaginary parts of the index of refraction for the material at the probe wavelength. The period of the oscillation is given by  $\lambda/(2n)$ . In general, the full form of the sensitivity function should be used in calculating the reflected probe signal. However, when  $\delta_1 \ll \lambda/(2n)$ , Eq. (22) reduces to the exponential form of  $f(z) = b \cdot \exp(-z/\delta_1)$  where  $b$  is a constant representing the coefficient of thermorefectance. Here we consider only the simple case of  $\delta_1 \ll \lambda/(2n)$ .

We first solve Eq. (10) for a semi-infinite solid heated by a pump beam with a total absorbed power  $P(t)$ , using an adiabatic boundary condition at the top surface. In the frequency domain, we obtain the temperature distribution in the material at radial position  $r$  and depth  $z$

$$\theta_s(\omega, r, z) = \int_0^\infty kJ_0(kr) \frac{\exp(-qz) - q\delta_0 \exp\left(-\frac{z}{\delta_0}\right)}{\Lambda_z q (1 - q^2 \delta_0^2)} \times \frac{P(\omega)}{2\pi} \exp\left(-\frac{k^2 w_0^2}{8}\right) dk. \quad (25)$$

For a probe laser with unit amplitude, the intensity distribution in the material is

$$I_{\text{probe}} = \frac{2}{\pi w_1^2 \delta_1} \exp\left(-\frac{2r^2}{w_1^2}\right) \exp\left(-\frac{z}{\delta_1}\right). \quad (26)$$

The frequency response  $H_s(\omega)$  of this semi-infinite solid is  $\theta_s(\omega, r, z)$  weighted by the probe intensity distribution along both the radial direction and the depth direction and then divided by  $P(\omega)$ . We then have

$$H_s(\omega) = \frac{1}{2\pi\delta_1} \int_0^\infty \int_0^\infty \int_0^\infty \frac{2}{\pi w_1^2} \exp\left(-\frac{2r^2}{w_1^2}\right) kJ_0(kr) 2\pi r dr \times \frac{\exp(-qz) - q\delta_0 \exp\left(-\frac{z}{\delta_0}\right)}{\Lambda_z q (1 - q^2 \delta_0^2)} \exp\left(-\frac{k^2 w_0^2}{8}\right) dk \times \exp\left(-\frac{z}{\delta_1}\right) dz, \quad (27)$$

which reduces to

$$H_s(\omega) = \frac{1}{2\pi} \int_0^\infty \frac{k(\delta_0 + \delta_1 + q\delta_0\delta_1)}{\Lambda_z q [1 + q(\delta_0 + \delta_1 + q\delta_0\delta_1)](\delta_0 + \delta_1)} \times \exp\left[-\frac{k^2(w_0^2 + w_1^2)}{8}\right] dk. \quad (28)$$

For frequencies  $\omega \gg \Lambda_z/[C_p(\delta_0 + \delta_1)^2]$ , Eq. (28) simplifies to

$$H_s(\omega) = \frac{1}{2\pi} \int_0^\infty \frac{k}{\Lambda_z q^2 (\delta_0 + \delta_1)} \exp\left[-\frac{k^2(w_0^2 + w_1^2)}{8}\right] dk, \quad (29)$$

which corresponds to the case where the thermal penetration depth is much smaller than the optical penetration depth. This high frequency limit also corresponds to the frequency range where the signal is most sensitive to the optical

absorption depth, which suggests that an effective absorption depth,  $\delta_{\text{eff}} \sim \delta_0 + \delta_1$ , can be used to approximate  $\delta_0$  in Eq. (20) and incorporate the effect of the optical penetration depth of the probe.

## D. Sensitivity to pump absorption depth

In this section, we examine the simple case of  $\delta_1 \ll \delta_0$  and  $L_e \ll \delta_0$  to study the sensitivity to  $\delta_0$ . The calculations here apply to FDTR measurements with cw lasers. For the case of TDTR, the sensitivity can be analyzed by inserting Eq. (20) into Eq. (4). In Fig. 4(a), we plot the calculated phase of  $H(\omega)$  as a function of frequency for a single crystal silicon substrate coated with a 100 nm transducer. In this calculation, we assumed a transducer heat capacity of  $2.5 \text{ MJ m}^{-3} \text{ K}^{-1}$ , a TBC of  $G = 100 \text{ MW m}^{-2} \text{ K}^{-1}$  between the transducer and the substrate, and pump and probe  $1/e^2$  spot radii of  $3 \mu\text{m}$ . The phase is calculated for three transducer thermal conductivities: 1, 10, and  $100 \text{ W m}^{-1} \text{ K}^{-1}$ , as labeled in the figure. We compare the results calculated with a 20 nm pump absorption depth (dashed lines) with those calculated with zero absorption depth, i.e., surface heating, (solid lines) for each thermal conductivity. In Fig. 4(b), we plot the sensitivity to the optical

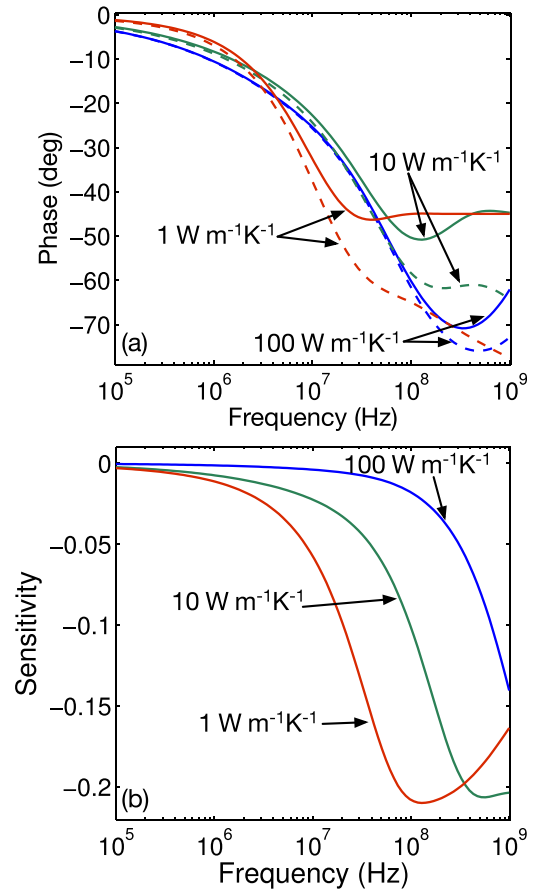


FIG. 4. (a) Calculated phase of  $H(\omega)$  for a silicon substrate coated by a 100 nm thick transducer over the frequency range of 100 kHz to 1 GHz. Solutions are shown for FDTR measurements with cw lasers using three thermal conductivities of the transducer:  $1 \text{ W m}^{-1} \text{ K}^{-1}$ ,  $10 \text{ W m}^{-1} \text{ K}^{-1}$ , and  $100 \text{ W m}^{-1} \text{ K}^{-1}$ . The dashed lines are calculated with a 20 nm pump laser absorption depth in the transducer, while the solid lines are calculated with surface heating. (b) Phase sensitivity to the 20 nm pump absorption depth calculated with the three thermal conductivities of the transducer.

absorption depth, computed as  $\partial\phi/\partial\delta_0$ , for these same three cases. For a transducer with a thermal conductivity of  $100 \text{ W m}^{-1} \text{ K}^{-1}$ , there is minimal difference between volumetric heating and surface heating until 100 MHz. Above 100 MHz, the heating period approaches the thermal time constant of the transducer,  $\tau_{th} \sim d^2 C_p / \Lambda$ , and the two models deviate from each other. For the lower thermal conductivity cases, the difference between surface and volumetric heating is larger and begins at lower frequencies. This comparison confirms the importance of accounting for the pump absorption in the transducer at high modulation frequencies and in measurements with low thermal conductivity transducers.

#### IV. MEASUREMENT OF AN AMORPHOUS SILICON FILM

To validate Eq. (20), we performed FDTR measurements of a 490 nm thick aSi film deposited on fused silica and single crystal silicon substrates. Our experimental system, described in Ref. 34, employs a 785 nm cw pump laser and a 532 nm cw probe laser. We chose to test the model on aSi because we expect a clear difference between surface heating and volumetric heating at frequencies well below 10 MHz due to the material's low thermal conductivity and weak optical absorption at 785 nm. In addition, the short phonon MFPs in aSi mean we do not have to consider complications arising from ballistic transport. We fit the measured phase data by performing a two-parameter fit of the thermal model, determining both the thermal conductivity and the effective optical absorption depth of the aSi film.

Figures 5(a) and 5(b) show the sample configurations during the measurement. The aSi thin film was deposited on the substrates by DC magnetron sputtering with a base pressure of  $10^{-8}$  mbar. The thickness of aSi was measured to be  $490 \pm 10$  nm via cross-sectional scanning electron microscopy. We measured the FDTR phase data directly from the aSi surface without a gold transducer layer. The focused pump and probe spot radii on the samples were  $2.8 \pm 0.03 \mu\text{m}$

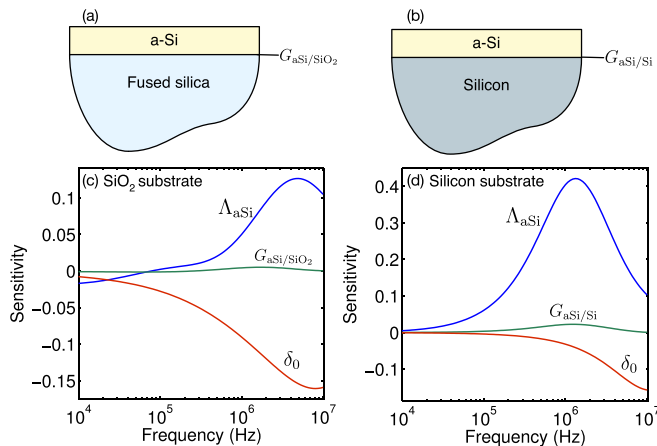


FIG. 5. (a) Sample configuration of aSi on fused silica. (b) Sample configuration of aSi on single crystal silicon. (c) Calculated phase sensitivity to  $\Lambda_{\text{aSi}}$ ,  $\delta_0$ , and the TBC between aSi and fused silica,  $G_{\text{aSi/SiO}_2}$ . (d) Calculated phase sensitivity to  $\Lambda_{\text{aSi}}$ ,  $\delta_0$ , and the TBC between aSi and single crystal silicon,  $G_{\text{aSi/Si}}$ .

TABLE II. Material properties used for calculating  $G_{\text{aSi/SiO}_2}$  and  $G_{\text{aSi/Si}}$ .

Material	$C_p$ ( $\text{MJ m}^{-3} \text{ K}^{-1}$ )	$v_t$ (m/s)	$v_l$ (m/s)	$\theta_D$ (K)
aSi	1.62 (Ref. 36)	3699 (Ref. 38)	8047 (Ref. 38)	487 (Ref. 39)
Si	1.65 (Ref. 37)	5332 (Ref. 40)	8970 (Ref. 40)	640 (Ref. 41)
SiO <sub>2</sub>	1.63 (Ref. 37)	2732 (Ref. 38)	4779 (Ref. 38)	470 (Ref. 42)

and  $2.3 \pm 0.02 \mu\text{m}$ , respectively, determined by a knife-edge measurement.

In Fig. 5(c), we consider the sample on fused silica and plot the calculated phase sensitivity to the thermal conductivity of aSi,  $\Lambda_{\text{aSi}}$ , the optical absorption depth of aSi at our pump wavelength,  $\delta_0$ , and the TBC of the aSi/SiO<sub>2</sub> interface,  $G_{\text{aSi/SiO}_2}$ . In Fig. 5(d), we show the same sensitivities for the sample on the silicon substrate. For these calculations, we assumed  $\Lambda_{\text{aSi}} = 1.4 \text{ W m}^{-1} \text{ K}^{-1}$  and  $\delta_0 = 300$  nm. The TBC values of the aSi/SiO<sub>2</sub> and aSi/Si interfaces were estimated using an empirically corrected diffuse mismatch model (DMM) that takes into account the Debye temperature ratios of the two materials.<sup>35</sup> The material properties used for the DMM calculation are listed in Table II where  $v_t$  and  $v_l$  are the transverse and longitudinal sound speeds, respectively, and  $\theta_D$  is the Debye temperature. The values are obtained as  $G_{\text{aSi/SiO}_2} = 173 \text{ MW m}^{-2} \text{ K}^{-1}$  and  $G_{\text{aSi/Si}} = 126 \text{ MW m}^{-2} \text{ K}^{-1}$ . We used literature values for the volumetric heat capacity of aSi,<sup>36</sup> fused silica,<sup>37</sup> and single crystal silicon,<sup>37</sup> each with a 3% uncertainty. The thermal conductivities of fused silica and single crystal silicon were taken from literature as well<sup>37</sup> with an uncertainty of 3%. Figures 5(c) and 5(d) show that the measurement is sensitive to both the thermal conductivity and absorption depth in aSi across much of the frequency range, and that the sensitivities are sufficiently different that it should be possible to uniquely determine both parameters. We see that the measurement is not sensitive to the TBC between aSi and the substrate. We then used the DMM calculated values with a 50% uncertainty for  $G_{\text{aSi/SiO}_2}$  and  $G_{\text{aSi/Si}}$  during the data fitting. For these properties, the high frequency limit condition of Eq. (28) is  $f = \omega/2\pi \gg 1.5$  MHz. Since this also corresponds to the frequency range where the signal is most sensitive to the optical absorption depth, we are justified in fitting the FDTR phase data with an effective optical absorption depth,  $\delta_{\text{eff}}$ , that is determined by the sum of the absorption depths at the pump and probe wavelengths.

In Fig. 6(a), we show the phase data for aSi on fused silica. We use  $\Lambda_{\text{aSi}}$  as the fitting parameter and show the best fit solution to the thermal model assuming the pump laser is absorbed on the surface. The surface heating model fails to capture the phase behavior through the entire frequency range, suggesting the need to model optical absorption in this low thermal conductivity material. We then fit the data with the volumetric heating model, Eq. (20), using  $\Lambda_{\text{aSi}}$  and  $\delta_{\text{eff}}$  as the fitting parameters. The results are shown in Fig. 6(b). This time the model produces a good fit to the phase data. The dashed lines are solutions obtained by varying the fitted value of  $\delta_{\text{eff}}$  by  $\pm 25\%$ . In Fig. 6(c), we show the phase data for aSi on single crystal silicon and the best fit to Eq. (20). The solution is again plotted as dashed lines by varying the  $\delta_{\text{eff}}$  values by  $\pm 25\%$ .



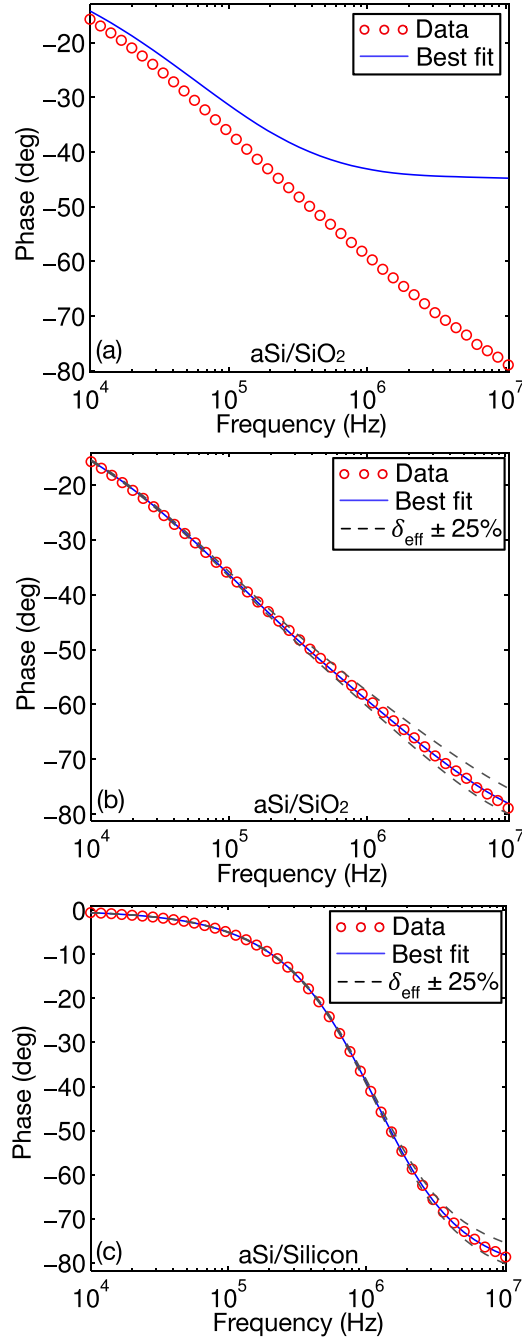


FIG. 6. (a) Measured phase data for aSi on fused silica and the best fit curve obtained with a surface heating model. (b) The same data with the best fit of the volumetric heating model of Eq. (20). Also shown are solutions obtained by varying the effective absorption depth by  $\pm 25\%$ . (c) Data and best fit for aSi on single crystal silicon.

The best fit values for  $\Lambda_{\text{aSi}}$  and  $\delta_{\text{eff}}$  are listed in bold in Tables III and IV, along with the literature values for the other parameters used in the model. The  $1/e$  confidence intervals were obtained with a Monte Carlo method described in Ref. 35 to account for the propagation of errors from known

TABLE III. Material properties for aSi on fused silica.

Material	$C_p$ (MJ m <sup>-3</sup> K <sup>-1</sup> )	$\Lambda$ (W m <sup>-1</sup> K <sup>-1</sup> )	$d$ (nm)	$\delta_{\text{eff}}$ (nm)
aSi	$1.62 \pm 0.05$ (Ref. 36)	<b><math>1.26 \pm 0.3</math></b>	$490 \pm 10$	<b><math>293 \pm 60</math></b>
SiO <sub>2</sub>	$1.63 \pm 0.05$ (Ref. 37)	$1.38 \pm 0.04$	$5 \times 10^5$	

TABLE IV. Material properties for aSi on single crystal silicon.

Material	$C_p$ (MJ m <sup>-3</sup> K <sup>-1</sup> )	$\Lambda$ (W m <sup>-1</sup> K <sup>-1</sup> )	$d$ (nm)	$\delta_{\text{eff}}$ (nm)
aSi	$1.62 \pm 0.05$ (Ref. 36)	<b><math>1.3 \pm 0.1</math></b>	$490 \pm 10$	<b><math>296 \pm 10</math></b>
Si	$1.65 \pm 0.05$ (Ref. 37)	$143 \pm 5$	$5 \times 10^5$	

parameters in the thermal model such as the heat capacity and film thickness. Our measured value of  $\Lambda_{\text{aSi}}$  agrees within 5% of the predicted thermal conductivity of aSi from literature.<sup>43</sup>

We compared the best fit value of  $\delta_{\text{eff}}$  with an independent measurement of the optical absorption depth obtained with a VASE ellipsometer. The amplitude and phase of light

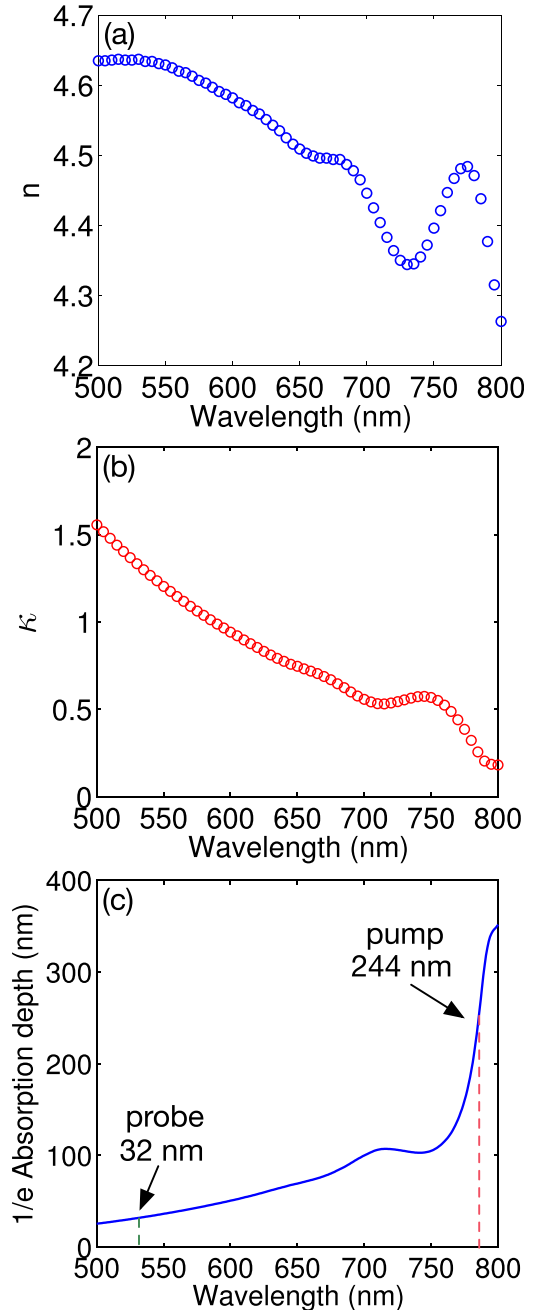


FIG. 7. (a) The real part  $n$  of the index of refraction of aSi. (b) The imaginary part  $\kappa$  of the index of refraction of aSi. (c) Calculated optical absorption depth of aSi.

reflected from the aSi sample surface were recorded at three incident angles: 55°, 60°, and 65°. We obtained the real part  $n$  and imaginary part  $\kappa$  of the index of refraction of the aSi film by fitting the ellipsometry data to a Cauchy dispersion model<sup>44</sup> with a thickness of 490 nm as the input parameter. The values for  $n$  and  $\kappa$  are plotted as a function of wavelength in Figs. 7(a) and 7(b), respectively. We then calculated the optical absorption depth as a function of wavelength using  $\delta = \lambda/(4\pi\kappa)$  where  $\lambda$  is the wavelength. The absorption depth is shown in Fig. 7(c). We see that the absorption depth at the pump wavelength of 785 nm is 244 nm, and that the absorption depth at the probe wavelength of 532 nm is 32 nm. Adding these gives an effective absorption depth of 276 nm, within 10% of the FDTR value of 296 nm.

## V. CONCLUSIONS

In conclusion, we have presented a thermal model for thermorefectance measurements that accounts for volumetric heating from laser absorption in the top layer of a sample. Sensitivity analysis suggests that the optical absorption depth of the pump laser has a significant effect on the signal at high frequencies and for low thermal conductivity transducers. Comparison of the volumetric heating model with FDTR measurements of amorphous silicon films on fused silica and single crystal silicon substrates showed good agreement, and allowed us to simultaneously measure the thermal conductivity and optical absorption depth of the amorphous silicon film, with good agreement to the literature value of thermal conductivity and the optical absorption depth obtained from ellipsometry. This model may be useful for understanding the limitations of a surface heating model at high modulation frequencies, interpreting thermorefectance measurements with low thermal conductivity transducers, and may enable nondestructive measurements of some samples by eliminating the need for a transducer layer.

## ACKNOWLEDGMENTS

We would like to thank Dr. V. V. Medvedev for providing the amorphous silicon samples. This work has been supported by the Trustees of Boston University.

<sup>1</sup>D. G. Cahill, P. V. Braun, G. Chen, D. R. Clarke, S. Fan, K. E. Goodson, P. Keblinski, W. P. King, G. D. Mahan, A. Majumdar, H. J. Maris, S. R. Phillpot, E. Pop, and L. Shi, *Appl. Phys. Rev.* **1**, 011305 (2014).

<sup>2</sup>C. A. Paddock and G. L. Eesley, *J. Appl. Phys.* **60**, 285 (1986).

<sup>3</sup>W. S. Capinski and H. J. Maris, *Rev. Sci. Instrum.* **67**, 2720 (1996).

<sup>4</sup>D. G. Cahill, *Rev. Sci. Instrum.* **75**, 5119 (2004).

<sup>5</sup>A. J. Schmidt, R. Cheaito, and M. Chiesa, *Rev. Sci. Instrum.* **80**, 094901 (2009).

<sup>6</sup>A. J. Schmidt, R. Cheaito, and M. Chiesa, *J. Appl. Phys.* **107**, 024908 (2010).

<sup>7</sup>D. G. Cahill, F. Watanabe, A. Rockett, and C. B. Vining, *Phys. Rev. B: Condens. Matter Mater. Phys.* **71**, 235202 (2005).

<sup>8</sup>M. N. Luckyanova, J. Garg, K. Esfarjani, A. Jandl, M. T. Bulsara, A. J. Schmidt, A. J. Minnich, S. Chen, M. S. Dresselhaus, Z. Ren, E. A. Fitzgerald, and G. Chen, *Science* **338**, 936 (2012).

<sup>9</sup>R. J. Stevens, A. N. Smith, and P. M. Norris, *J. Heat Transfer* **127**, 315 (2005).

<sup>10</sup>H.-K. Lyee and D. Cahill, *Phys. Rev. B* **73**, 144301 (2006).

<sup>11</sup>B. C. Gundrum, D. G. Cahill, and R. S. Averback, *Phys. Rev. B: Condens. Matter Mater. Phys.* **72**, 245426 (2005).

<sup>12</sup>A. J. Minnich, J. A. Johnson, A. J. Schmidt, K. Esfarjani, M. S. Dresselhaus, K. A. Nelson, and G. Chen, *Phys. Rev. Lett.* **107**, 95901 (2011).

<sup>13</sup>Y. Hu, L. Zeng, A. J. Minnich, M. S. Dresselhaus, and G. Chen, *Nat. Nanotechnol.* **10**, 701 (2015).

<sup>14</sup>K. T. Regner, D. P. Sellan, Z. Su, C. H. Amon, A. J. McGaughey, and J. A. Malen, *Nat. Commun.* **4**, 1640 (2013).

<sup>15</sup>Y. Wang, J. Y. Park, Y. K. Koh, and D. G. Cahill, *J. Appl. Phys.* **108**, 43507 (2010).

<sup>16</sup>W. Hsieh and D. G. Cahill, *J. Appl. Phys.* **109**, 113520 (2011).

<sup>17</sup>R. B. Wilson, B. A. Apgar, L. W. Martin, and D. G. Cahill, *Opt. Express* **20**, 28829 (2012).

<sup>18</sup>R. B. Wilson and D. G. Cahill, *Nat. Commun.* **5**, 5075 (2014).

<sup>19</sup>K. T. Regner, L. C. Wei, and J. A. Malen, *J. Appl. Phys.* **118**, 235101 (2015).

<sup>20</sup>K. C. Collins, A. A. Maznev, J. Cuffe, K. A. Nelson, and G. Chen, *Rev. Sci. Instrum.* **85**, 124903 (2014).

<sup>21</sup>J. Liu, G. Choi, and D. G. Cahill, *J. Appl. Phys.* **116**, 233107 (2014).

<sup>22</sup>V. V. Medvedev, J. Yang, A. J. Schmidt, A. E. Yakshin, R. W. E. van de Kruijs, E. Zoethout, and F. Bijkerk, *J. Appl. Phys.* **118**, 085101 (2015).

<sup>23</sup>J. Yang, E. Ziade, C. Maragliano, R. Crowder, X. Wang, M. Stefancich, M. Chiesa, A. K. Swan, and A. J. Schmidt, *J. Appl. Phys.* **116**, 023515 (2014).

<sup>24</sup>A. J. Schmidt, X. Chen, G. Chen, and M. Chiesa, *Rev. Sci. Instrum.* **79**, 114902 (2008).

<sup>25</sup>R. B. Wilson, J. P. Feser, G. T. Hohensee, and D. G. Cahill, *Phys. Rev. B* **88**, 144305 (2013).

<sup>26</sup>A. Majumdar and P. Reddy, *Appl. Phys. Lett.* **84**, 4768 (2004).

<sup>27</sup>C. Kittel, *Introduction to Solid State Physics*, 8th ed. (John Wiley & Sons, Inc., 2005), pp. 146–149.

<sup>28</sup>R. H. M. Groeneveld, R. Sprik, and A. Lagendijk, *Phys. Rev. B* **51**, 11433 (1995).

<sup>29</sup>J. P. Girardeau-Montaut, M. Afif, C. Girardeau-Montaut, S. D. Moustakizis, and N. Papadogiannis, *Appl. Phys. A: Mater. Sci. Process.* **62**, 3 (1996).

<sup>30</sup>M. V. Kampen, J. T. Kohlhepp, W. J. M. D. Jonge, B. Koopmans, and R. Coehoorn, *J. Phys.: Condens. Matter* **17**, 6823 (2005).

<sup>31</sup>E. D. Palik, *Handbook of Optical Constants of Solids* (Academic Press, Orlando, 1985).

<sup>32</sup>H. S. Carslaw and J. C. Jaeger, *Conduction of Heat in Solids* (Oxford University Press, Oxford, England, 1959).

<sup>33</sup>C. Thomsen, H. Grahm, H. Maris, and J. Tauc, *Phys. Rev. B* **34**, 4129 (1986).

<sup>34</sup>J. Yang, C. Maragliano, and A. J. Schmidt, *Rev. Sci. Instrum.* **84**, 104904 (2013).

<sup>35</sup>E. Ziade, J. Yang, G. Brummer, D. Nothorn, T. Moustakas, and A. J. Schmidt, *Appl. Phys. Lett.* **107**, 091605 (2015).

<sup>36</sup>J. S. Custer, M. O. Thompson, D. C. Jacobson, J. M. Poate, S. Roorda, W. C. Sinke, and F. Spaepen, *Appl. Phys. Lett.* **64**, 437 (1994).

<sup>37</sup>D. R. Lide, in *CRC Handbook of Chemistry and Physics*, edited by D. R. Lide (Taylor & Francis, Boca Raton, FL, 2007).

<sup>38</sup>J. M. Larkin and A. J. H. McGaughey, *Phys. Rev. B* **89**, 144303 (2014).

<sup>39</sup>B. L. Zink, R. Pietri, and F. Hellman, *Phys. Rev. Lett.* **96**, 055902 (2006).

<sup>40</sup>E. T. Swartz and R. O. Pohl, *Rev. Mod. Phys.* **61**, 605 (1989).

<sup>41</sup>N. W. Ashcroft and D. N. Mermin, *Solid State Physics* (Harcourt College, New York, 1976).

<sup>42</sup>H. Wang, Y. Xu, M. Shimono, Y. Tanaka, and M. Yamazaki, *Mater. Trans.* **48**, 2349 (2007).

<sup>43</sup>P. B. Allen and J. L. Feldman, *Phys. Rev. Lett.* **62**, 645 (1989).

<sup>44</sup>Y. C. Liu, J. H. Hsieh, and S. K. Tung, *Thin Solid Films* **510**, 32 (2006).